Periodica Polytechnica Electrical Engineering and Computer Science, 69(4), pp. 386–400, 2025

Artificial Intelligence DTC MTPA Strategy Based on Speed MRAS Observer for Electric Vehicle Traction Applications

Norediene Aouadj[1*], Kada Hartani[2], Abdelkader Merah[2]

[1] Second Cycle Department, Higher School of Electrical and Energetic Engineering (ESGEEO), Chemin Vicinal 9, 31000 Oran, Algeria
[2] Electrotechnical Engineering Laboratory, Electrotechnical Department, Faculty of Technology, University of Saida Dr. Moulay Tahar, 20000 Ennasr, Saida, P.O.B. 138, Algeria
[*] Corresponding author, e-mail: aouadj.norediene@esgee-oran.dz

Received: 22 May 2025, Accepted: 04 December 2025, Published online: 16 December 2025

Abstract

This paper presents an advanced direct torque control (DTC) strategy incorporating artificial intelligence and a speed Model Reference Adaptive System (MRAS) observer for permanent magnet synchronous motors (PMSMs) used in electric vehicle traction. The studied electric vehicle is equipped with four in-wheel PMSMs, requiring an electric differential to ensure balanced torque distribution and vehicle stability, especially during cornering maneuvers. To reduce system weight and enhance efficiency, two machines on the same vehicle side are powered by a single three-leg inverter, forming a multi-machine single-inverter configuration. A master–slave control structure is adopted to manage this architecture and ensure synchronized operation of all motors. The proposed AI-based DTC combined with the MRAS speed observer significantly improves torque accuracy, dynamic response, and robustness against disturbances. Simulation results obtained using MATLAB/Simulink confirm that the proposed strategy achieves high performance in both transient and steady-state conditions, ensuring reliable traction, enhanced vehicle stability, and improved overall dynamic behavior.

Keywords

artificial intelligence, direct torque control, electric vehicle traction, in-wheel motor, sliding mode control, MRAS observer

1 Introduction

Electric vehicles equipped with in-wheel motors offer significant advantages in energy efficiency and precise motion control. Recent research has increasingly focused on advanced motion control strategies – such as yaw stability control and traction control – made possible by the independent actuation of each in-wheel motor [1–4].

In-wheel motor technology enables highly responsive and precise torque actuation, offering significant advantages for advanced electric vehicle (EV) traction systems [5–7]. Unlike industrial motors, EV traction motors must withstand frequent start–stop cycles, rapid acceleration and deceleration, and deliver high torque at low speeds for hill climbing while maintaining efficient low-torque operation at high cruising speeds. Consequently, these motors must ensure fast and robust torque dynamics over a wide speed range to meet instantaneous driver torque demands, while maintaining extremely low torque ripple – typically below ±2% – to avoid undesirable vibrations, noise, and reduced driving comfort [8].

Permanent magnet synchronous motors (PMSMs) are widely regarded as the leading candidates for electric vehicle (EV) propulsion systems due to their high efficiency, superior power and torque density, wide constant-power speed range, robust mechanical structure, and overall cost-effectiveness. However, the mitigation of torque ripple remains a critical challenge for their effective deployment in traction applications. Excessive torque ripple not only degrades ride comfort through undesirable vibrations but can also induce mechanical stresses and negatively affect vehicle stability. Consequently, significant research efforts continue to focus on advanced control strategies and motor design optimizations aimed at minimizing torque ripple in PMSM-based electric drivetrains [8].

Recently, direct torque control (DTC) of PMSM drives has gained wide attention in industrial and electric vehicle applications for its simple structure, fast dynamics, and robustness. Conventional DTC, however, suffers from high torque ripple due to hysteresis-based switching and

Cite this article as: Aouadj, N., Hartani, K., Merah, A. "Artificial Intelligence DTC MTPA Strategy Based on Speed MRAS Observer for Electric Vehicle Traction Applications", Periodica Polytechnica Electrical Engineering and Computer Science, 69(4), pp. 386–400, 2025. https://doi.org/10.3311/PPee.41104

limited voltage vector selection, which can degrade drivability through vibrations and acoustic noise. To address this, the present work proposes an enhanced Sliding Mode Backstepping DTC (SMB-DTC) for in-wheel PMS motors, offering improved dynamic response and substantially reduced torque ripple under varied operating conditions.

The studied electric vehicle employs four in-wheel PMSMs in a direct-drive configuration, powered *via* a five-leg three-phase inverter controlling parallel bi-PMS motor pairs. This setup enables precise, independent torque control at each wheel, enhances vehicle stability and handling, and allows coordinated participation of the traction motors during braking and regenerative energy recovery [9].

Sensorless control of PMSM drives has attracted considerable attention, with the Model Reference Adaptive System (MRAS) emerging as a widely adopted method for AC drive applications [10–12]. This work implements MRAS-based sensorless speed control for a DTC-driven PMSM powered by a NPC inverter [13].

Electric vehicles (EVs) are increasingly favored for their zero emissions, smooth and quiet operation, and enhanced safety, yet challenges such as limited energy density and long charging times remain. Advanced control strategies, particularly those integrating artificial intelligence (AI), are crucial for optimizing performance by identifying optimal system parameters [14, 15].

El Ouanjli et al. [16] reviewed various DTC strategies for induction motors, incorporating fuzzy logic, neural networks, sliding mode control, and genetic algorithms to enhance efficiency. These methods were evaluated based on complexity, parameter sensitivity, torque ripple reduction, switching losses, and speed-tracking performance. Selecting the optimal strategy depends on application requirements, hardware availability, reliability, and cost. Additionally, an ANN-based DTC for fuel cell EVs modulates stator flux according to torque demand to maximize driving performance. This study focuses on the control efficacy of IM drives for EV propulsion, without considering full vehicle dynamics, range, or energy efficiency [17].

The electric differential advances beyond conventional mechanical designs by eliminating inter-wheel mechanical links, reducing drivetrain weight and friction, and enhancing power transmission efficiency and reliability. It independently supplies traction to each wheel and limits its power to inner wheels *via* speed controllers [18]. This work develops an electric differential for the studied EV using a sliding mode backstepping control strategy.

In that respect, we propose in this paper a direct torque control (DTC) technique integrating artificial intelligence for an all-wheel drive electric vehicle. This paper is organized as follows:

- Section 2 presents the sensorless DTC-MTPA approach, including the IPMSM mathematical model, conventional DTC, MTPA control technique, and MRAS-based speed observer;
- Section 3 details the design of the AI-enhanced DTC controller;
- Section 4 describes the vehicle dynamic model and electric differential to ensure full reproducibility of the simulations;
- Section 5 discusses the simulation results;
- Conclusions are provided in Section 6.

2 Principal DTC approach

2.1 IPMSM mathematical model

The model of the IPMSM in the stationary *α–β* reference frame is described by Eqs. (1) to (6) [19, 20].

The stator flux linkage is comprised of:

$$\begin{cases} \dfrac{di_{s\alpha}}{dt} = -\dfrac{R_s}{L_s} i_{s\alpha} + \dfrac{\Phi_f}{L_s}\omega_m \sin\theta + \dfrac{1}{L_s} v_{s\alpha} \\ \dfrac{di_{s\beta}}{dt} = -\dfrac{R_s}{L_s} i_{s\beta} - \dfrac{\Phi_f}{L_s}\omega_m \cos\theta + \dfrac{1}{L_s} v_{s\beta} \\ \dfrac{d\omega_m}{dt} = -\dfrac{f}{J}\omega_m + \dfrac{3}{2}\dfrac{p^2\Phi_f}{J}\begin{pmatrix} -i_{s\alpha}\sin\theta \\ +i_{s\beta}\cos\theta \end{pmatrix} - \dfrac{p}{J}C_r \end{cases} . \tag{1}$$

The torque equation can is defined as:

$$T_{em} = \frac{3}{2}p\left(\Phi_d i_q - \Phi_q i_d\right) = \frac{3}{2}p\left[\left(L_d - L_q\right)i_d i_q + \Phi_f i_q\right]. \tag{2}$$

The mechanical equation is expressed by:

$$J\frac{d\Omega}{dt} + f\Omega = T_{em} - T_L, \tag{3}$$

where:

$$\omega_m = p\Omega, \tag{4}$$

$$T_e = T_L + f\omega_m + J\frac{d\omega_m}{dt}, \tag{5}$$

where T_{load} is the load torque, f is the viscous coefficient of friction, and $J = J_m + J_\omega$ is the moment of inertia of the motor and the wheel.

A structural of a coupling between mechanics and motorization as shown in Fig. 1. The expressions of the resistant torques which act on each wheel are given by:

$$T_{\text{load}_i} = R_\omega F_{t_i} - d_z F_{z_i},\ \ i = 1,\ldots,4. \tag{6}$$

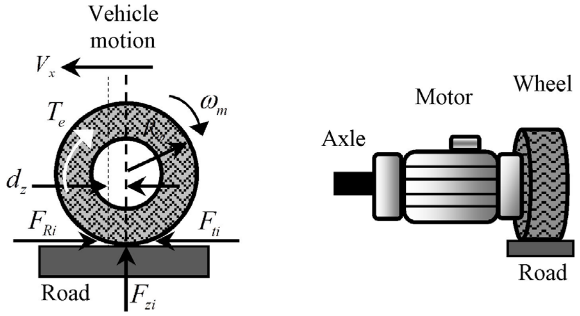

Fig. 1 Coupling between mechanics and motorization

2.2 Conventional direct torque control

Achieving optimal control performance in this specific system is dependent on the successful implementation of the DTC strategy. DTC utilizes non-linear hysteresis controllers to directly control torque and flux. Unlike alternative control strategies, DTC eliminates the requirement for reference transformation in order to independently control flux and torque.

Instead, the machine's currents are indirectly controlled through torque and flux control. For a visual representation (Fig. 2), which illustrates the block diagram of the DTC control method.

In a stationary frame $\alpha\beta$, by carefully choosing the appropriate voltage vectors, it is possible to regulate the flux trajectory and speed. In the realm of hysteresis comparators, different levels are commonly incorporated, such as the utilization of a two-level comparator for the flux controller and a three-level comparator for the torque controller.

In order to determine the components of the stator flux linkage, the prescribed procedure is utilized [21].

$$\begin{cases} \Phi_{s\alpha} = \int_0^t \left(V_s - R_s i_{s\alpha}\right) dt \\ \Phi_{s\beta} = \int_0^t \left(V_s - R_s i_{s\beta}\right) dt \end{cases} \tag{7}$$

Through the careful analysis of these elements, in addition to considering several other variables, it becomes possible to ascertain the amplitude of the stator flux linkage.

$$\Phi_s = \sqrt{\Phi_{s\alpha}^2 + \Phi_{s\beta}^2} \tag{8}$$

Minimizing ripple in torque and flux linkage is essential for enhancing the performance of the DTC system. A successful strategy integrates this method with MTPA, a well-recognized technique celebrated for its rapid dynamic response and exceptional efficiency [22].

2.3 MTPA control technique

The DTC method necessitates the reference values for torque and flux. Incorporating speed loop control removes the requirement for direct torque calculation. To enhance efficiency, the reference flux is established based on motor parameters and reference torque, which influences the controlling current. Once the stator current is transformed into the synchronous frame (i_d, i_q) and parameters such as the rotor magnet flux linkage constant Φ_f and the ***d*** and ***q***

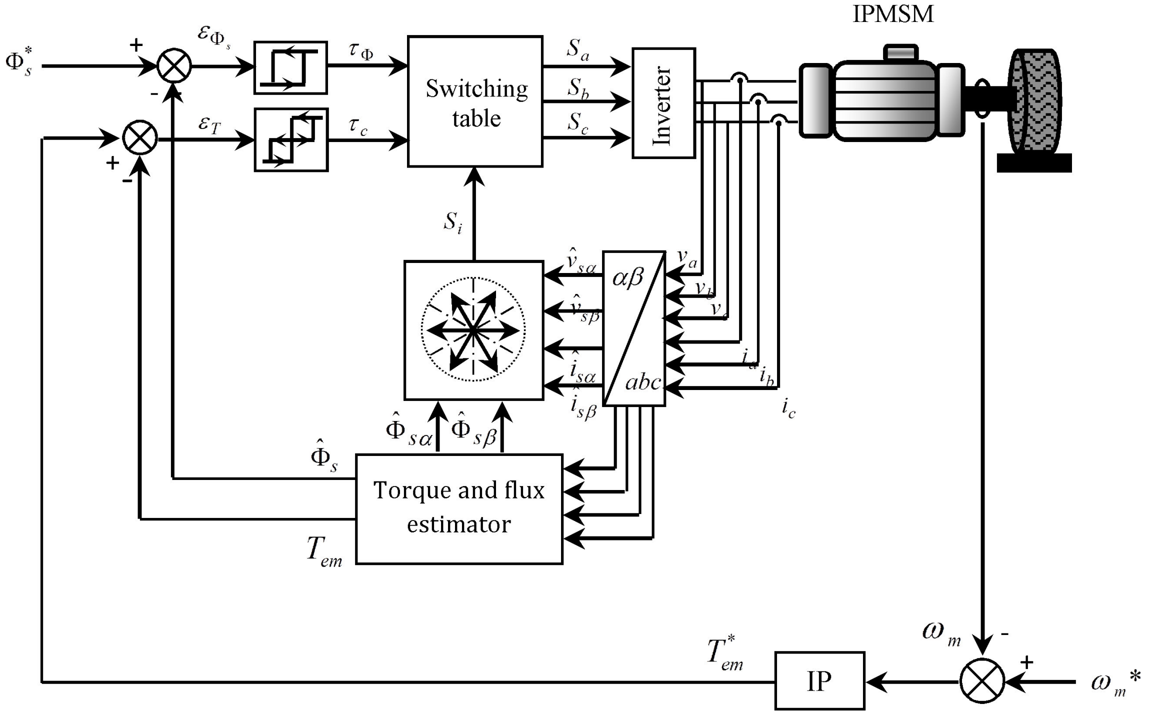

Fig. 2 Direct torque control block diagram of IPMSM

axis inductances (L_d, L_q) are known, the calculation for the reference flux proceeds as follows [23, 24]:

$$\Phi_s^* = \sqrt{\left(\Phi_f + L_d i_{d_{\text{MTPA}}}\right)^2 + \left(L_q i_{q_{\text{MTPA}}}\right)^2}. \tag{9}$$

To achieve optimal torque output based on a specific current, it is essential to examine Eq. (2) which represents the electromagnetic torque generated by the motor. The currents in the ***d***- and ***q***-axes can be expressed as:

$$i_d = \hat{I}_s \cos\beta, \tag{10}$$

$$i_q = \hat{I}_s \sin\beta, \tag{11}$$

In Fig. 3 [25], the "torque angle" (β) is defined as the angle between the stator phase current vector and the positive direction of the ***d***-axis, while $\hat{I}_s$ represents the magnitude of the stator phase current in an IPM motor [25].

The developed torque in IPMSM motors can be viewed as a combination of the magnet's excitation torque T_{mag} and the reluctant torque T_{rel}, as shown in Fig. 4. This is because the q-axis reactance/inductance is larger than the ***d***-axis reactance/inductance, resulting i.e., $L_q > L_d$. The expression for the developed torque is as follows in Eq. (12) [25]:

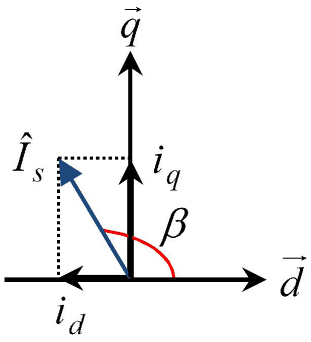

Fig. 3 Torque angle

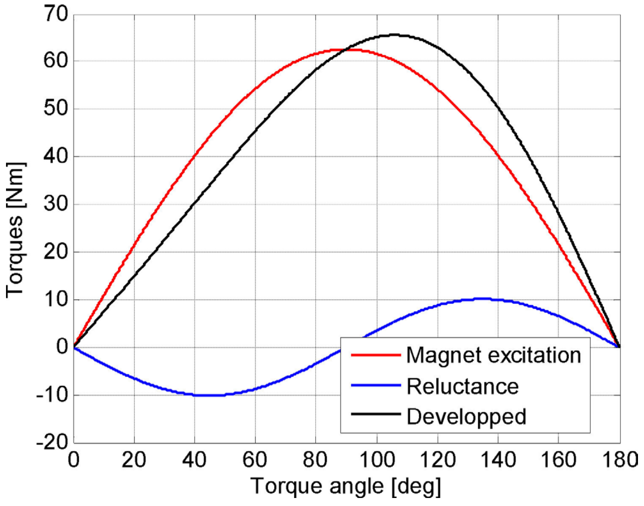

Fig. 4 Developed torque vs. torque angle of IPMSM [26]

$$T_e = T_{mag} + T_{rel}, \tag{12}$$

where:

$$T_{mag} = \frac{3}{2} p \Phi_f \hat{I}_s \sin\beta, \tag{13}$$

$$T_{rel} = \frac{3}{2} p \left(L_d - L_q\right) \hat{I}_s^2 \frac{\sin 2\beta}{2}. \tag{14}$$

In the constant-torque region of an IPMSM, the maximum torque per ampere (MTPA) strategy identifies the optimal ***d***- and ***q***-axis current combination to maximize torque output for traction applications. Below the base speed, torque is limited only by the current, without inducing voltage stress, and the ***d***-axis current is mathematically defined as in Eq. (15):

$$i_q = \sqrt{i_s^2 - i_d^2}, \tag{15}$$

Replace Eq. (15) with Eq. (2):

$$\frac{\partial C_{em}}{\partial i_d}\left(i_{d_{\text{MTPA}}}\right) = 0. \tag{16}$$

The ***d***-axis current during MTPA operation is obtained as follows in Eq. (17):

$$i_{d_{\text{MTPA}}} = \frac{\Phi_f}{4\left(L_d - L_q\right)} - \sqrt{\frac{\Phi_f^2}{16\left(L_d - L_q\right)^2} + \frac{\hat{I}_s^2}{2}}. \tag{17}$$

By substituting Eq. (16) into Eq. (14), it is possible to derive the ***q***-axis current in MTPA operation with simplicity.

$$i_{q_{\text{MTPA}}} = \sqrt{\hat{I}_s^2 - i_{d_{\text{MTPA}}}^2} \tag{18}$$

When the current drops below $\hat{I}_s$, the operating point on the MTPA curve shifts downward. At the base speed ω_b defined by the intersection of the current-limit circle and the voltage–limit ellipse – the motor reaches its maximum allowable current and voltage.

$$i_{d_{\max}} = -\frac{\Phi_f}{4\left(L_d - L_q\right)} - \sqrt{\frac{\Phi_f^2}{16\left(L_d - L_q\right)^2} + \frac{\hat{I}_{\max}^2}{2}} \tag{19}$$

$$i_{q_{\max}} = \sqrt{\hat{I}_{\max}^2 - i_{d_{\max}}^2} \tag{20}$$

We will than give:

$$\omega_b = \frac{V_{sn}}{p\sqrt{\left(\Phi_f + L_d i_{d_{\max}}\right)^2 + \left(L_q i_{q_{\max}}\right)^2}}. \tag{21}$$

When opting to surpass the base speed while still adhering to the MTPA control strategy, the operating point is established at the point where the new voltage ellipse intersects with the MTPA curve [27].

$$i_{dt} = \frac{L_q^2 - 2L_qL_d + 2L_d^2}{2\left(L_q - L_d\right)\left(L_q^2 + L_d^2\right)}\Phi_f - \sqrt{\frac{\left(L_q^2 - 2L_qL_d + 2L_d^2\right)^2}{4\left(L_q - L_d\right)^2\left(L_q^2 + L_d^2\right)^2}\Phi_f^2 + \frac{\left(\dfrac{V_{sn}}{p\omega_r}\right)^2 - \Phi_f^2}{L_q^2 + L_d^2}} \tag{22}$$

$$i_{qt} = \sqrt{i_{dt}^2 - \frac{\Phi_f}{\left(L_q - L_d\right)}i_{dt}} \tag{23}$$

By utilizing Eq. (24), one can determine the highest attainable speed.

$$\omega_{\text{end,MTPA}} = \frac{V_{sn}}{p\Phi_f} \tag{24}$$

When operating at this speed, the motor exhibits no torque or power.

2.4 Speed MRAS observer

The MRAS estimates rotor speed sensorlessly by comparing a reference IPMSM model with an adjustable stator-current-based model [28–31], using the resulting error to iteratively refine the speed estimate.

The reference model represents the IPMSM, while the adjustable model is based on the stator current equations, enabling the implementation of a sensorless control algorithm (Fig. 5) [32].

A PI controller enhances the MRAS adaptation by using the estimated rotor speed to adjust the stator-current-based model. Continuous negative feedback on the speed error ensures system stability. The IPMSM current is given by Eq. (25):

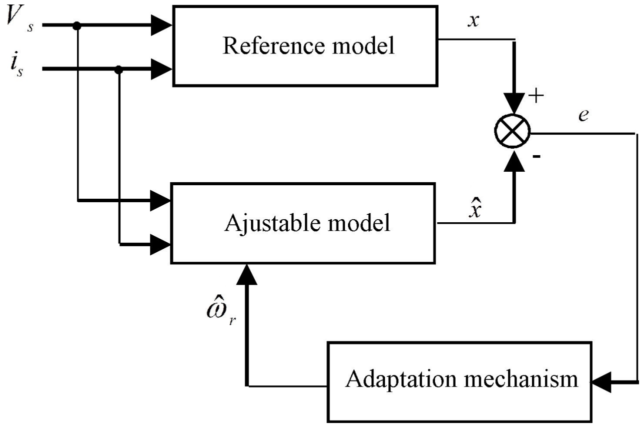

Fig. 5 Structure of Model Reference Adaptive System

$$\begin{cases} \dfrac{di_d}{dt} = -\dfrac{R_s}{L_s}i_d + \dfrac{L_q}{L_s}i_q\omega_r + \dfrac{1}{L_s}v_d \\ \dfrac{di_q}{dt} = -\dfrac{R_s}{L_s}i_q - i_d\omega_r - \dfrac{\Phi_f}{L_s}\omega_r + \dfrac{1}{L_s}v_q \end{cases}. \tag{25}$$

One way to express the current equations mentioned above is as follows in Eq. (26):

$$\frac{d}{dt}\begin{bmatrix} i'_d \\ i'_q \end{bmatrix} = \begin{bmatrix} -\dfrac{R_s}{L_d} & \dfrac{\omega_r L_q}{L_d} \\ -\dfrac{\omega_r L_d}{L_q} & -\dfrac{R_s}{L_q} \end{bmatrix}\begin{bmatrix} i'_d \\ i'_q \end{bmatrix} + \begin{bmatrix} \dfrac{1}{L_d} & 0 \\ 0 & \dfrac{1}{L_q} \end{bmatrix}\begin{bmatrix} v'_d \\ v'_q \end{bmatrix}, \tag{26}$$

where:

$$\begin{cases} i'_d = i_d + \dfrac{\Phi_f}{L_d} \\ i'_q = i_q \\ v'_d = v_d + \dfrac{R_s\Phi_f}{L_d} \\ v'_q = v_q \end{cases}. \tag{27}$$

The adjustable model utilizes Eq. (26) with speed as the variable. The reference model for this algorithm is the IPMSM, which provides i_d and i_q. To calculate the estimated value of the rotor speed, the algorithm takes into account the information from the reference model.

$$\hat{\omega}_r = \left(k_p + \frac{k_i}{s}\right)\left[-\frac{L_q}{L_d}\left(i'_q - \hat{i}'_q\right)\hat{i}'_d + \frac{L_d}{L_q}\left(i'_d - \hat{i}'_d\right)\hat{i}'_q\right] + \hat{\omega}_r(0) \tag{28}$$

A PI controller is employed in the MRAS observer to adjust the adaptive model to match the reference model, minimizing the error toward zero and ensuring accurate rotor speed estimation.

3 DTC strategy based artificial intelligence

Fig. 6 illustrates the DTNC control for IPMSM motor drive. The network receives inputs such as e_T, which represent the error between the torque generated by the motor and their respective reference values; e_Φ, the error related to the modulus of the stator flux versus a reference generated by MTPA strategy; and θ_s, which indicates the position of the stator flux vector in the complex plane

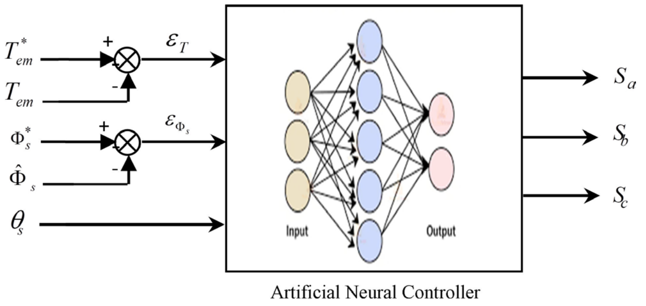

Fig. 6 Neural controller structure for DTC control

(α, β).The outputs consist of the pulses S_a, S_b, S_c, which are essential for driving the converter to ensure proper motor feeding. During the training phase of the network, utilizing data derived from the simulation of the traditional DTC control, the output is generated through a calculation that propagates from the input layer to the output layer once the input data is presented. The quadratic sum of the errors is calculated using Eq. (29):

$$E(k) = \frac{1}{N}\sum_{i=1}^{N}\left(d_i(k) - y_i(k)\right)^2. \tag{29}$$

Let d_i represent the desired output, y_i denote the computed output, k signify the number of iterations, and N indicate the size of the training dataset. As a result, through the use of the error backpropagation method, the error is transmitted from the outputs back toward the inputs, resulting in adjustments to the network's synaptic weights as described in Eq. (30):

$$w_{ji}(k+1) = w_{ji}(k) - \eta\frac{dE(k)}{dw_{ji}(k)}. \tag{30}$$

In this context, w_{ji} represents the weight linked to the connection between the j-th neuron and the i-th neuron of the previous layer, while η signifies the learning rate. The features of the network are described as follows:

- The structure includes two hidden layers, each containing 10 neurons, in addition to input and output layers that have 3 neurons each;
- Both input and output layers use linear (purelin) activation functions, whereas the hidden layers employ a sigmoid (logsig) function;
- This setup follows a supervised learning approach, utilizing the backpropagation of error as its selected learning algorithm;
- The chosen optimization method is the Levenberg-Marquardt technique, noted for its rapidity and efficiency in convergence.

3.1 Sliding mode controller design

In order to optimize the dynamic performance of the sliding mode speed controller and reduce the occurrence of chattering, it is essential to incorporate the reaching law technique. The exponential reaching law, as mentioned in Liu and Wang [33] and in Ning et al. [34], is the specific reaching law that is employed for this purpose.

$$\dot{s} = -\varepsilon \operatorname{sgn}(s) - ks,\ \ \varepsilon > 0,\ \ k > 0 \tag{31}$$

Equation (31) yields a solution when $s > 0$:

$$s(t) = -\frac{\varepsilon}{k} + \left(s_0 + \frac{\varepsilon}{k}\right)e^{-kt},\ \ s_0 = s(0). \tag{32}$$

Once t reaches a certain threshold, the speed at which the sliding surface is reached surpasses that predicted by the exponential function. To calculate the duration, it takes to reach the sliding surface, the equation $s(t) = 0$ can be utilized.

$$t = \frac{1}{k}\left[\ln\left(s_0 + \frac{\varepsilon}{k}\right) - \ln\left(\frac{\varepsilon}{k}\right)\right] \tag{33}$$

By directly adjusting the parameters ε and k, one can effectively control the speed at which reaching occurs. Incorporating the reaching law into the sliding mode control system offers several advantages, including maintaining dynamic performance during the reaching phase and reducing system chattering. The state variables of the system adhere to the specifications detailed in Ning et al. [34].

$$\begin{aligned} x_1 &= \omega^* - \omega \\ x_2 &= \dot{x}_1 = \dot{\omega}^* - \dot{\omega} \end{aligned} \tag{34}$$

We can represent the reference speed of the motor as ω^*, and the actual speed of the motor as $\omega = \omega_m/p$. The system's sliding surface can be defined as follows in Eq. (35):

$$s = cx_1 + x_2,\ \ c > 0. \tag{35}$$

Therefore, we have:

$$\dot{s} = c\dot{x}_1 + \dot{x}_2 = 2 + \dot{\omega}^* + \frac{f}{J}\dot{\omega} - \frac{T_{em}^*}{J}. \tag{36}$$

In order to obtain the sliding mode controller, we can proceed by implementing the following approach:

$$T_{em}^* = J\int\left(cx_2 + \ddot{\omega}^* + \frac{f}{J}\dot{\omega} + \varepsilon \operatorname{sgn}(s) + ks\right)dt, \tag{37}$$

where T_{em}^* is the required reference torque.

It can be inferred from Eq. (37) that the integral term can act as a filter and attenuate the chattering effect in the sliding mode control.

We choose $V_1 = (1/2)s^2$ as the Lyapunouv function. The time derivative of function V_1 is as follows:

$$\dot{V}_1 = s\dot{s} = s\left(-\varepsilon\,\mathrm{sgn}\left(s\right) - ks\right). \tag{38}$$

The system is stable according to the Lyapunouv stability criterion. Therefore, the negative semi-effective of function $\dot{V}_1$ can be guaranteed by an approximation choice of the parameters $\varepsilon > 0$ and $k > 0$, which results in the opposite of the parameters signs for s and $\dot{s}$ [34].

4 Vehicle dynamic model

The electric vehicle (EV) studied is equipped with four in-wheel permanent magnet synchronous motors (PMSMs), one in each wheel, as illustrated in Fig. 7. This configuration enables precise, independent control of each wheel's torque for optimal vehicle motion management. Two in-wheel PMSMs are connected in parallel to a single inverter powered by a DC source and controlled *via* a sensorless direct torque neural control (DTNC) scheme, as shown in Fig. 8.

The assumptions underlying the dynamics of the four-wheel drive vehicle depicted in Fig. 8 include an even distribution of load across all four wheels, the front wheels functioning as the steering wheels, a transverse road angle assumed to be zero, and the vehicle's center of gravity (CG) frame being perfectly aligned with the longitudinal axis. To evaluate the forces acting on the vehicle, we analyze the frame (x, y) with the front wheels set at a steering angle δ. The forces at the contact points between the wheels and the ground are illustrated in Fig. 9.

The equations that describe a vehicle's longitudinal, lateral, and yawing movements are formulated as follows in Eq. (39) [35]:

$$\begin{aligned}
&M_v\left(\dot{v}_x - rv_y\right) = \sum_{i=0}^{4} F_{xi}\cos\delta_i \\
&-\sum_{i=0}^{4} F_{yi}\sin\delta_i - 0,5\rho S_f C_{px} v_x^2 - M_v g\sin\alpha_p, \\
&M_v\left(\dot{v}_y + rv_x\right) = \sum_{i=0}^{4} F_{xi}\sin\delta_i \\
&+\sum_{i=0}^{4} F_{yi}\cos\delta_i - 0,5\rho S_f C_{px} v_x^2 + M_v g\sin\alpha_p, \\
&J_v\dot{r} = \sum_{i=0}^{4} F_{xi}\sin\delta_i x_i + \sum_{i=0}^{4} F_{yi}\cos\delta_i x_i - \sum_{i=0}^{4} F_{xi}\cos\delta_i y_i \\
&+\sum_{i=0}^{4} F_{xi}\sin\delta_i y_i + \sum_{i=0}^{4} M_{ai} + 0,5\rho S_f C_{px} v_x^2.
\end{aligned} \tag{39}$$

The overall impact of the F_x operating in the direction (x), which includes both the aerodynamic force and the resistance from the slope to be climbed, can be represented as:

$$\begin{aligned}
&F_x = \sum_{i=0}^{4} F_{xi}\cos\left(\delta_i\right) - \sum_{i=0}^{4} F_{yi}\sin\left(\delta_i\right) \\
&-0.5\rho S_f C_{px} v_x^2 - M_v g\sin\left(\alpha_p\right).
\end{aligned} \tag{40}$$

The outcome of the forces in relation to the direction (y) can be represented by:

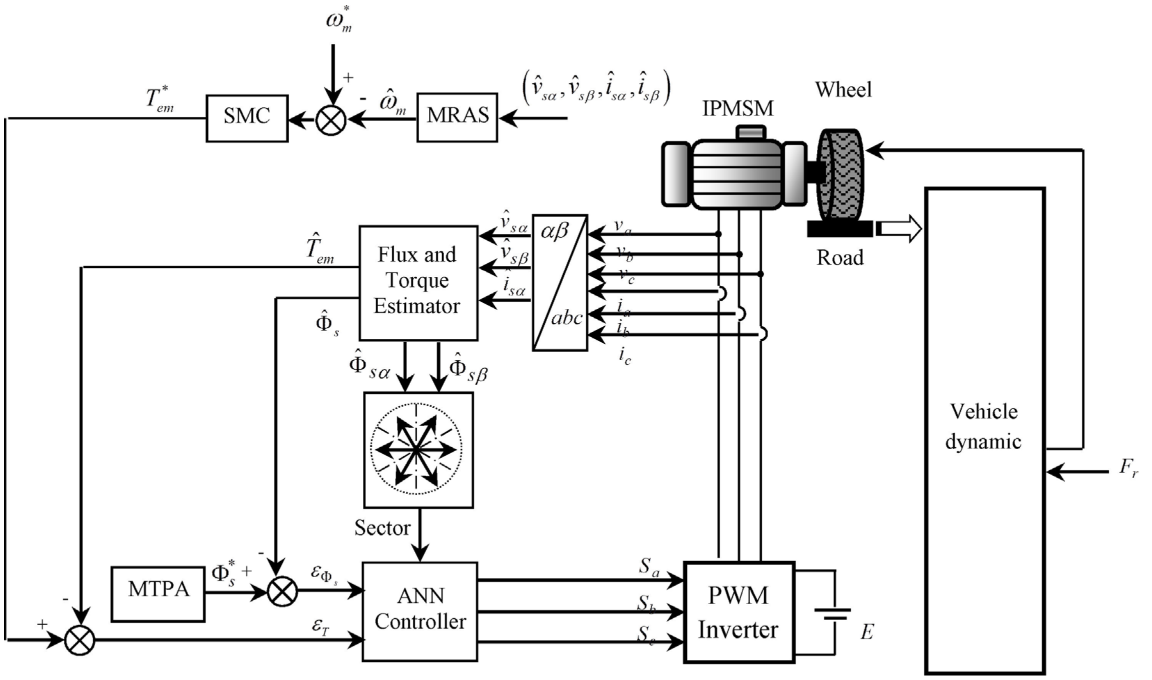

Fig. 7 Block diagram of the new sensorless MTPA-DTNC with SMC

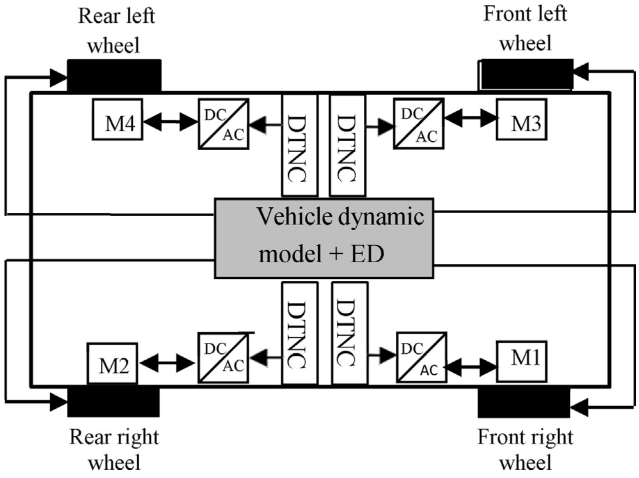

Fig. 8 Configuration of the EV with four independent in-wheel-motors

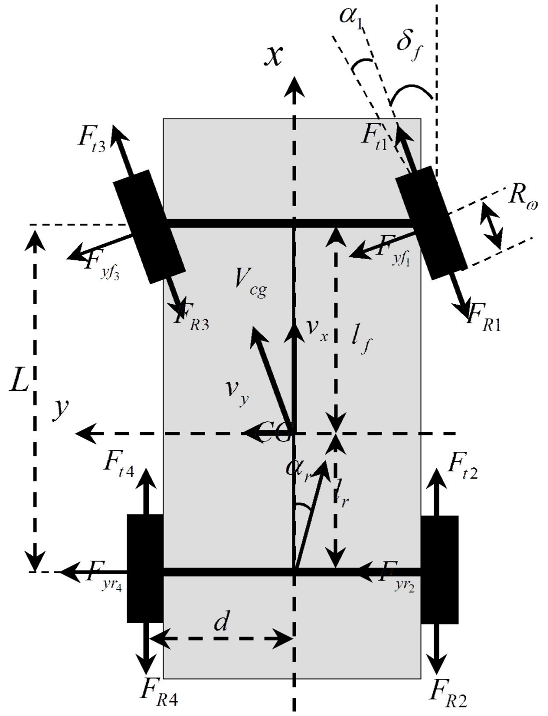

Fig. 9 Vehicle Dynamics Model

$$F_y = \sum_{i=0}^{4} F_{xi} \sin(\delta_i) + \sum_{i=0}^{4} F_{yi} \cos(\delta_i) \\ +0.5\rho S_f C_{px} v_y^2 + M_v g \sin(\alpha_p). \tag{41}$$

Equation (42) illustrates the moment of the forces that are acting along the (*z*) axis:

$$M_z = \sum_{i=0}^{4} F_{xi} \sin(\delta_i) x_i + \sum_{i=0}^{4} F_{yi} \cos(\delta_i) x_i \\ -\sum_{i=0}^{4} F_{xi} \cos(\delta_i) y_i + \sum_{i=0}^{4} F_{yi} \sin(\delta_i) y_i \\ +\sum_{i=0}^{4} M_{ai} + 0.5\rho S_f C_{M_z} v^2. \tag{42}$$

The linear velocities for the four wheels can be expressed as:

$$\begin{aligned} u_{t1} &= (v_x + dr)\cos(\delta) + (v_y + l_f r)\sin(\delta), \\ u_{t2} &= v_x + dr, \\ u_{t3} &= (v_x - dr)\cos(\delta) + (v_y + l_f r)\sin(\delta), \\ u_{t4} &= v_x - dr. \end{aligned} \tag{43}$$

The loads from the rear and front axles at the wheel contact points can be simplified in the following manner:

$$\begin{aligned} F_{z1} &= \frac{L_r g M_v}{2L} - \frac{h_{cg} M_v}{2L}(\dot{V}_x - rV_y) + \frac{h_{cg} M_v}{2l_w}(\dot{V}_y + rV_x), \\ F_{z3} &= \frac{L_r g M_v}{2L} - \frac{h_{cg} M_v}{2L}(\dot{V}_x - rV_y) - \frac{h_{cg} M_v}{2l_w}(\dot{V}_y + rV_x), \\ F_{z2} &= \frac{L_f g M_v}{2L} - \frac{h_{cg} M_v}{2L}(\dot{V}_x - rV_y) + \frac{h_{cg} M_v}{2l_w}(\dot{V}_y + rV_x), \\ F_{z4} &= \frac{L_f g M_v}{2L} - \frac{h_{cg} M_v}{2L}(\dot{V}_x - rV_y) - \frac{h_{cg} M_v}{2l_w}(\dot{V}_y + rV_x). \end{aligned} \tag{44}$$

The slip angle α_i is defined in relation to a steering angle δ_i as follows in Eq. (45):

$$\alpha_i = \beta_i - \delta_i. \tag{45}$$

The steering angle of the wheel (*i*), denoted as β_i, is defined by the subsequent equation (Eq. (46)):

$$\beta_i \arctan\left(\frac{v_{yi}}{v_{xi}}\right) = \arctan\left(\frac{v_y + \dot{\psi} x_i}{v_y + \dot{\psi} x_i}\right). \tag{46}$$

The sideslip for both the front and rear wheels is outlined as follows in Eq. (47):

$$\begin{cases} \alpha_1 = \arctan\left(\dfrac{1}{V_x + d}(V_y + rL_f)\right) - \delta \\ \alpha_3 = \arctan\left(\dfrac{1}{V_x - d}(V_y + rL_f)\right) - \delta \\ \alpha_2 = \arctan\left(\dfrac{1}{V_x - d}(V_y + rL_r)\right) \\ \alpha_4 = \arctan\left(\dfrac{1}{V_x - d}(V_y + rL_r)\right) \end{cases}, \tag{47}$$

where L_f is the distance from the gravity center to front axle, L_r is the distance from the gravity center to rear axle, δ is the Steering angle of the front wheels.

The coefficient of longitudinal adhesion, denoted as μ_a, for a wheel is defined as:

$$\mu_a = \frac{F_x}{F_z}. \tag{48}$$

4.1 Electric differential system design

The operational concept behind an electric differential system mirror that of a conventional mechanical differential. As an electric vehicle approaches a turn, the outer wheels cover longer distances compared to the inner wheels, indicating that the rotational speed of the outer wheels exceeds that of the inner ones. An electric differential system automatically adjusts for the speed variations between these inner and outer wheels. Consequently, the structure of the electric vehicle features four in-wheel motors, specifically permanent magnet synchronous motors, installed in each wheel, as illustrated in Fig. 10. This particular setup allows for independent speed adjustments for each in-wheel motor $\omega_{2ref} \neq \omega_{4ref}$.

The electric converter's structure enables individual control of these motors without any coupling through the control system. This results in effective rejection of disturbances and a system that operates similarly to controlling a single motor. Additionally, the implementation of an electric differential system is facilitated by the speed control of the driving wheels, as depicted in Fig. 10 [35].

5 Simulation and discussion

5.1 Test 1

In Section 5.1, we present the results from simulations conducted with the sensorless MTPA-DTNC setup in conjunction with a sliding mode speed controller. This cutting-edge control method has been assessed using a speed reference of 400 rad/s. The parameters for the IPMSM employed in the electric vehicle's traction system are detailed in Table 1.

Fig. 11 illustrates the system's performance utilizing the proposed method. The motor initiates operation at a reference speed of 400 rad/s. To assess the controller's robustness, the load torque is incrementally adjusted from 15 to 20 N m at $t = 0.4$ s. The dynamic performance of the sensorless MTPA-DTNC IPMSM drive, controlled by the SMC speed controller, is depicted in Fig. 11. This controller has been evaluated across a broad spectrum of motor speeds. The findings presented in Fig. 11 indicate that the motor starts with an initial load torque of 15 Nm and successfully reaches the commanded speed of 400 rad/s. Ultimately, the controller undergoes testing for disturbances caused by step load torque changes.

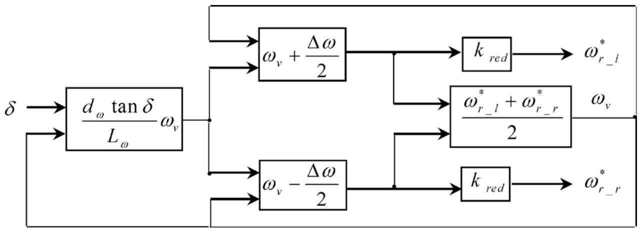

Fig. 10 Electric differential scheme

Table 1 IPMSM parameters used in EV application

Symbol	Parameter	Value
P_e	Nominal power	30 kW
$\hat{T}_e$	Maximal torque	65.55 N m
V_s	Line to line voltage	230 V
R_s	Stator resistance	0.45 Ω
L_d	d-axis inductance	0.54 mH
L_q	q-axis Inductance	1.05 mH
Φ_f	Permanent magnet flux linkage	0.148 Wb
p	Number of pole pairs	3
$\hat{I}_s$	Nominal current	100 A
ω_{base}	Based speed	466.81 rad/s
$\omega_{\mathrm{end}_{\mathrm{MTPA}}}$	MTPA limited speed	518.02 rad/s

Simulation results shown in Fig. 11 provide the evidence of improvements of the proposed MTPA-DTNC strategy over the conventional DTC by indicating a fast torque response, and an accurate speed tracking performance. Fig. 11 (a) show the speed response. The actual speed converges with reference speed in very short time with a negligible overshoot and no steady state error. The sliding mode controller rejects the load disturbance rapidly and converges back the reference speed. The proposed senroless MTPA-DTNC method gives a better response of the stator flux linkage during transient-state. Fig. 11 (c) and (d) show the stator flux response. Fig. 11 (c) shows that the stator flux magnitude was constant at its nominal value 0.148 Wb generated by MTPA strategy.

Fig. 11 (e) and (f) show, in more detail, the stator current and phase current of IPMSM motor, during steps of speed command and load torque. It was observed, that the MTPA-DTNC has better performance using SMC speed controller. Fig. 11 (e) and (f) show that the stator current which increases when load disturbance is applied.

Result shows that the torque and flux ripples are decreased in MTPA-DTNC and provide good speed tracking performance compared with the conventional DTC.

5.2 Test 2

The target vehicle responses are determined according to the driver's inputs, including steering commands and the desired vehicle speed. Table 2 provides a comprehensive summary of the vehicle's key parameters and their corresponding numerical values, which serve as the basis for simulating and evaluating the dynamic behavior of the electric vehicle.

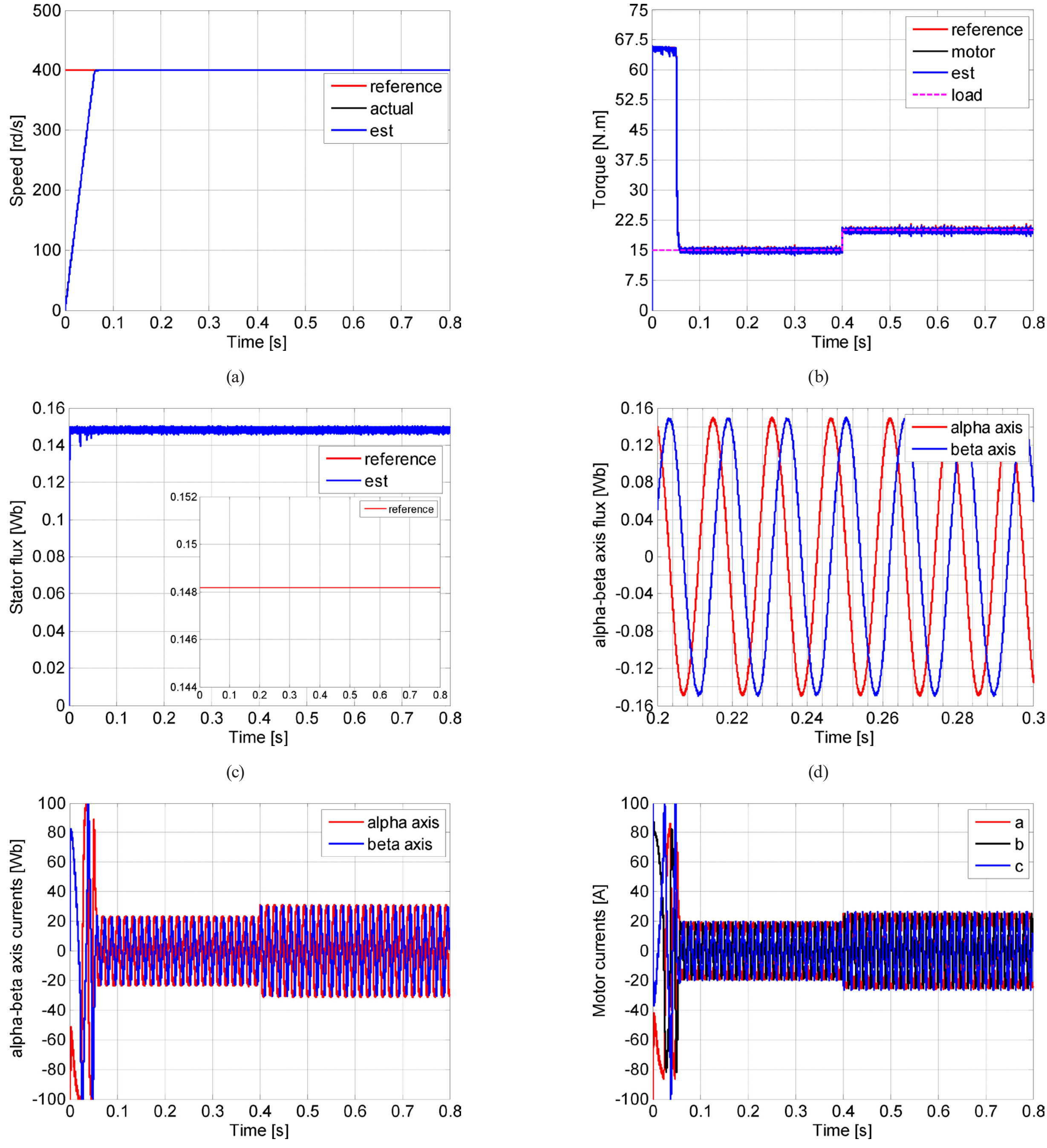

(a) (b)

(c) (d)

(e) (f)

Fig. 11 Simulation results Test 1: (a) speed; (b) torque; (c) stator flux; (d) alpha-betta axis flux; (e) alpha-betta axis currents; (f) motor currents [26]

The accelerator pedal input defines a baseline reference speed for the vehicle. This common reference speed is then adjusted based on the steering angle to determine the individual reference speeds for the left and right in-wheel motors. When the steering angle is zero, the vehicle moves along a straight path, and the electronic differential remains inactive. However, during a turn, the steering input causes the electronic differential to modulate the speed distribution among the four in-wheel motors, ensuring that the outer wheels rotate faster than the inner wheels. This dynamic adjustment enhances vehicle stability and handling while navigating curved trajectories.

The vehicle starts from rest and accelerates to a predetermined reference speed. Fig. 12 (a) depicts the steering angle input used as the reference for the simulations. The vehicle initiates a right turn at $t = 6$ s, reaching the peak steering angle at $t = 7.5$ s, which is maintained for approximately four seconds before gradually returning to zero at $t = 11.5$ s. Subsequently, at $t = 13.5$ s, a left turn is executed, with the steering angle peaking at $t = 15$ s, sustained for about four

Table 2 Notation and vehicle parameters

Symbol	Quantity	Value
M_v	Vehicle mass	1562 kg
J_v	Vehicle inertia	2630 kg m^2
J_ω	Wheel inertia	1.284 kg m^2
L_f	Distance from the gravity center to front axle	1.104 m
L_r	Distance from the gravity center to rear axle	1.421 m
h_{cg}	Height gravity center of the vehicle	0.5 m
S_f	Frontal area of vehicle	2.04 m^2
ρ	Air density	1.2 kg m^{-3}
C_{px}	Drag coefficient	0.25
C_{rr}	Rolling resistance coefficient	0.01
C_f	Longitudinal stiffness of each tire lateral	37407 N/rad
C_r	Lateral stiffness of each tire lateral	51918 N/rad
R_ω	Wheel radius	0.294 m

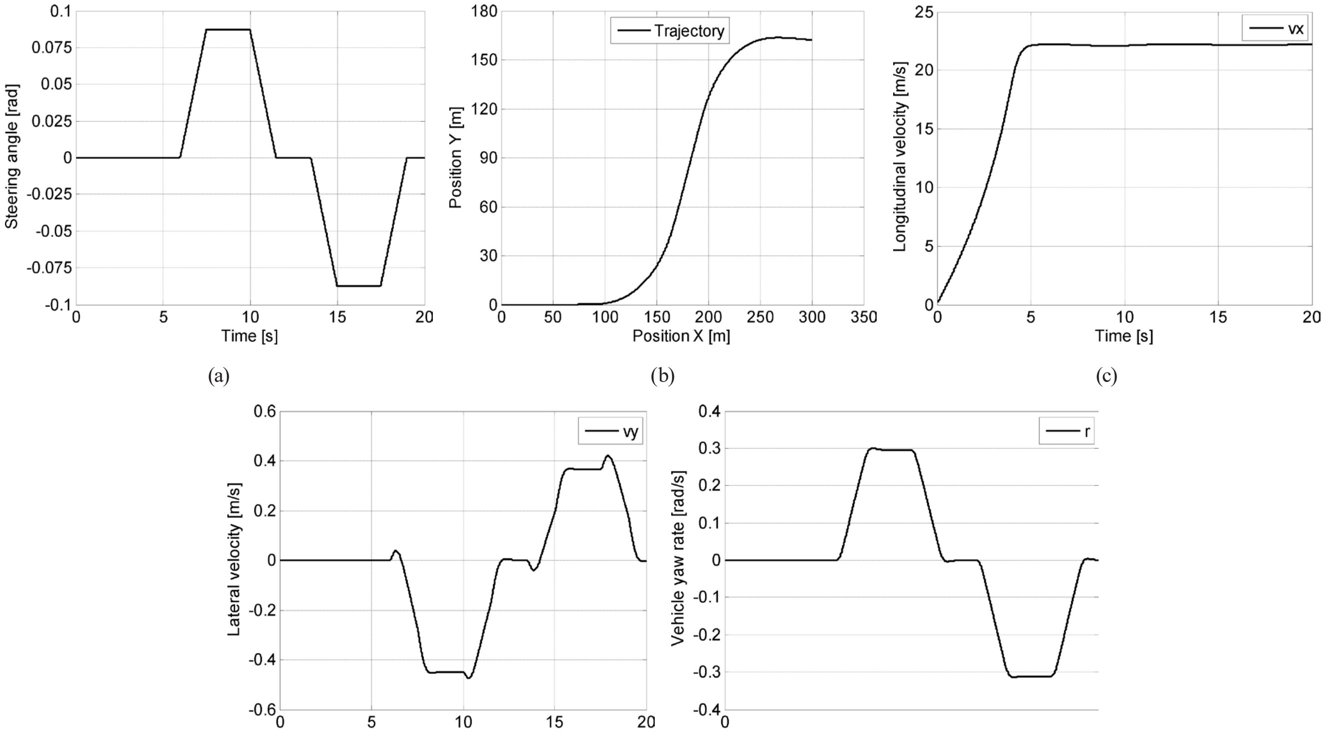

(a) (b) (c)

(d) (e)

Fig. 12 Simulation results Test 2: (a) steering angle; (b) trajectory; (c) longitudinal velocity; (d) lateral velocity; (e) vehicle yaw rate [26]

seconds, and then returning to zero at $t = 19$ s. This steering profile ensures a dynamic evaluation of the vehicle's response under successive turning maneuvers.

Fig. 12 (c) presents the vehicle's longitudinal velocity, clearly illustrating its acceleration and steady-state behavior. The lateral velocity *vy* and yaw rate *r*, shown in Fig. 12 (d) and 12 (e), are directly affected by the driver's steering input. These dynamic responses are only observed during cornering maneuvers and vanish when the vehicle travels along a straight trajectory, reflecting the vehicle's coordinated lateral and rotational motion under steering-induced forces.

Fig. 13 (c) depicts the variation in traction forces generated by the front axle motors (M1 and M3) in comparison with the rear axle motors (M2 and M4) during a turning maneuver. At the onset, all motors produce substantial traction forces to overcome the vehicle's inertia and resistive forces, including rolling resistance and aerodynamic drag. This coordinated force distribution ensures sufficient acceleration while maintaining vehicle stability

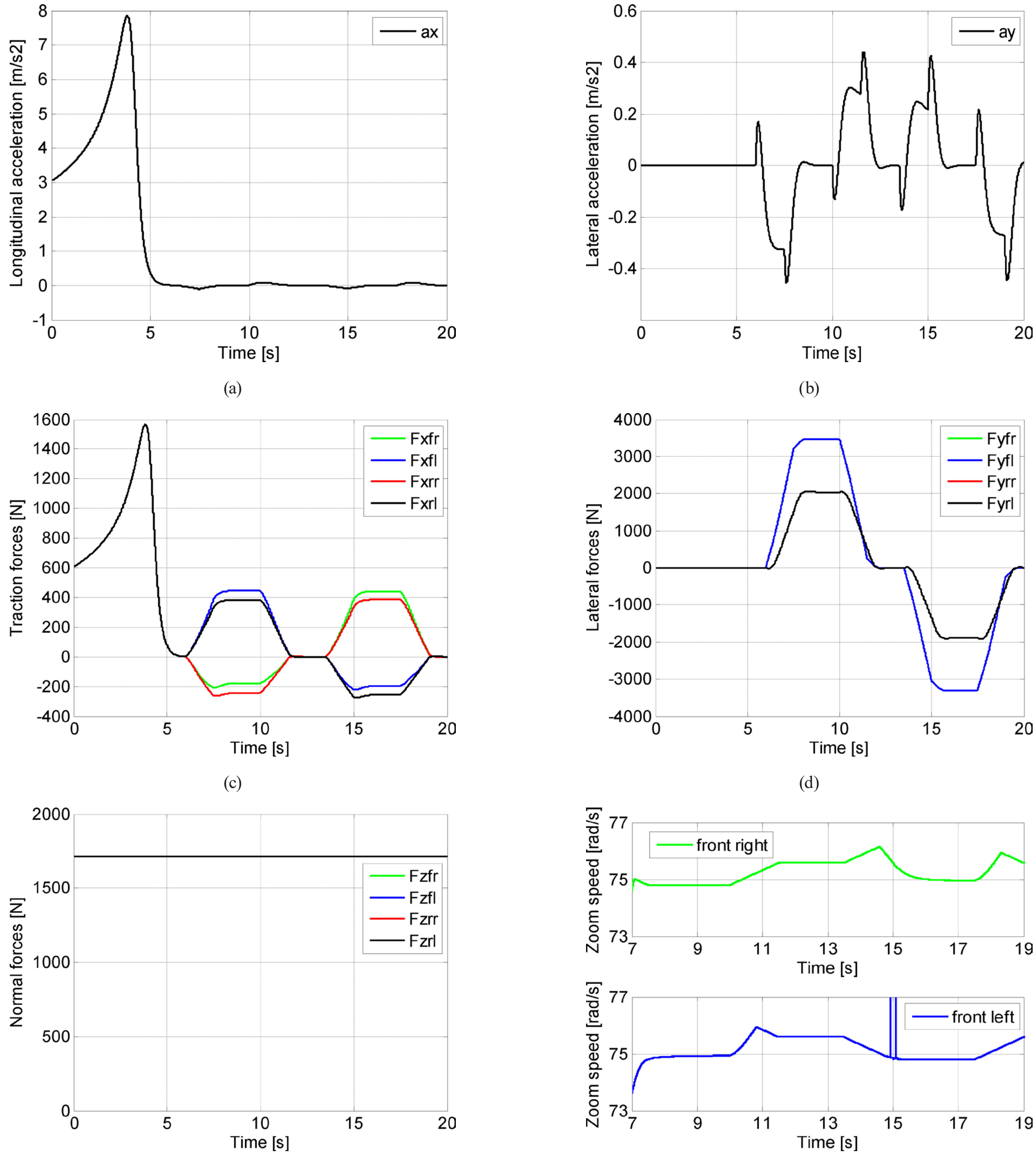

(a) (b)

(c) (d)

(e) (f)

Fig. 13 Simulation results Test 2: (a) longitudinal acceleration; (b) lateral acceleration; (c) traction forces; (d) lateral forces; (e) normal forces; (f) motors speed [26]

throughout the turn. Notably, the differential allocation of traction between the front and rear motors contributes to optimized handling and cornering performance.

Fig. 13 (f) presents the rotational speeds of the in-wheel motors. During straight-line motion, all four motors exhibit nearly identical speed profiles, converging to steady-state values as the vehicle accelerates. When the vehicle enters a turn, a distinct speed differentiation emerges: the outer motors (M1 and M2) rotate faster than the inner motors (M3 and M4) to accommodate the longer travel distance along the curvature. This adaptive speed distribution, managed by the electric differential, ensures precise torque allocation and contributes to enhanced vehicle stability and handling during cornering.

Fig. 14 (a) illustrates the variation in the electromagnetic torque of the in-wheel motors. During vehicle startup,

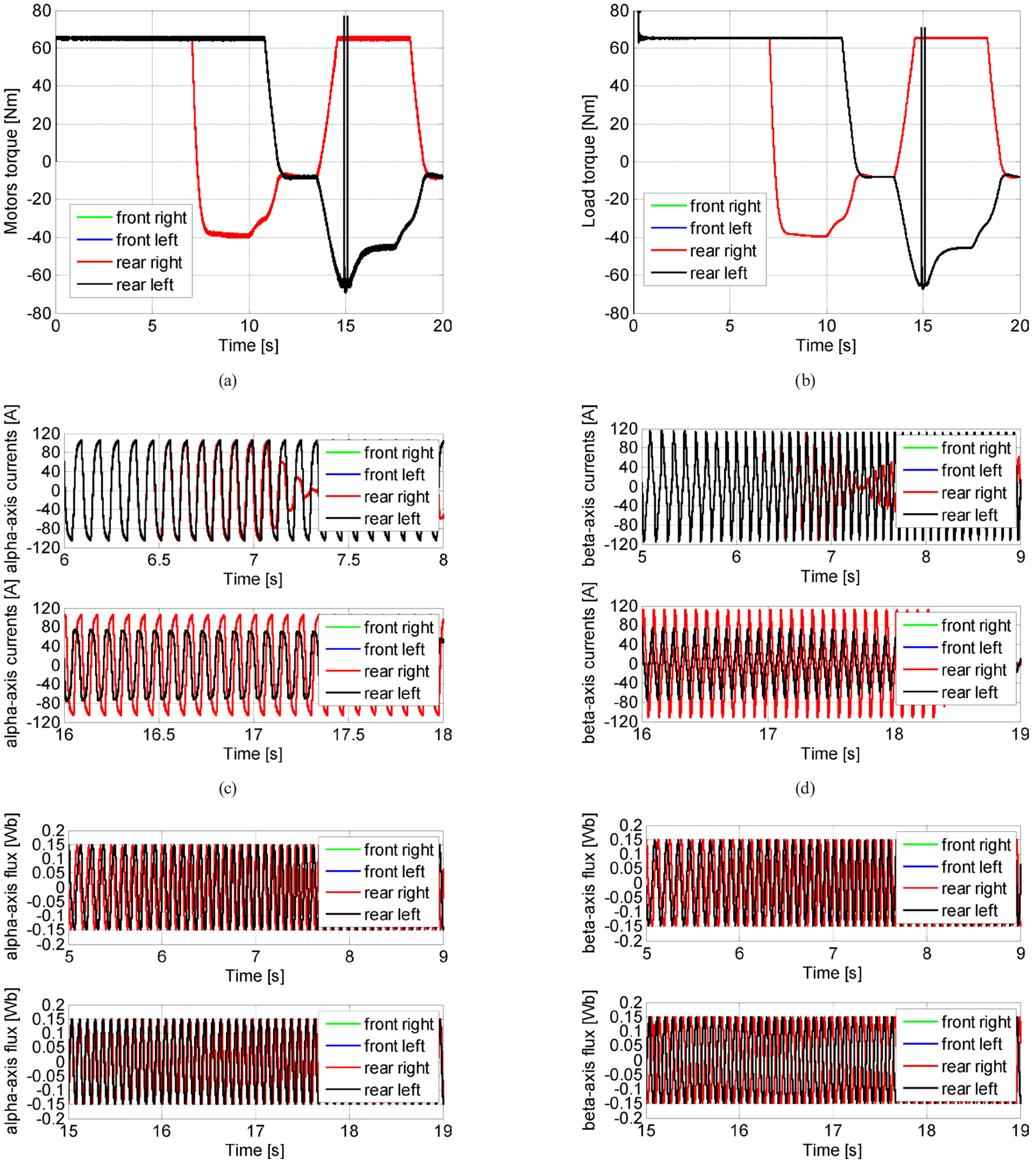

(a) (b) (c) (d) (e) (f)

Fig. 14 Simulation results Test 2 : (a) motors torque; (b) load torque; (c) alpha-axis currents; (d) betta- axis currents; (e) alpha- axis flux; (f) betta-axis flux [26]

all motors generate high torque to overcome initial inertia and resistive forces, maintaining elevated levels until the wheels reach steady-state speeds. Once stabilized, the torques gradually decrease to their respective set points. During cornering, a clear torque differentiation is observed: the outer motors (M3 and M4) produce higher electromagnetic torque than the inner motors (M1 and M2) to accommodate the larger travel distance along the turn. This torque distribution aligns with the vehicle's dynamic requirements, ensuring optimal traction, stability, and efficient cornering performance.

The simulation results demonstrate that the proposed control strategy effectively governs a traction system comprising four in-wheel motors, delivering excellent performance in both steady-state and dynamic conditions. The approach ensures coordinated torque and speed distribution across all wheels, achieving robust stability, precise wheel-speed tracking, and smooth vehicle motion, even under varying driving scenarios and steering maneuvers.

6 Conclusion

This paper presents a sensorless direct torque control (DTC) strategy incorporating artificial intelligence for an all-wheel-drive electric vehicle. By integrating artificial neural networks with a speed MRAS observer, the proposed method achieves fast, precise, and robust torque and speed control with accurate setpoint tracking under varying road conditions. Simulation results demonstrate that the MTPA-DTNC scheme, coupled with an electric differential, effectively enhances torque smoothness, dynamic response, and overall vehicle stability, highlighting its suitability for advanced electric vehicle traction applications.

References

[1] Hori, Y. "Future vehicle driven by electricity and Control-research on four-wheel-motored "UOT electric march II"", IEEE Transactions on Industrial Electronics, 51(5), pp. 954–962, 2004. https://doi.org/10.1109/TIE.2004.834944

[2] Esmailzadeh, E., Vossoughi, G. R., Goodarzi, A. "Dynamic Modeling and Analysis of a Four Motorized Wheels Electric Vehicle", Vehicle System Dynamics, 35(3), pp. 163–194, 2001. https://doi.org/10.1076/vesd.35.3.163.2047

[3] Magallan, G. A., De Angelo, C. H., Garcia, G. O. "Maximization of the Traction Forces in a 2WD Electric Vehicle", IEEE Transactions on Vehicular Technology, 60(2), pp. 369–380, 2011. https://doi.org/10.1109/TVT.2010.2091659

[4] Sakai, S., Sado, H., Hori, Y. "Motion control in an electric vehicle with four independently driven in-wheel motors", IEEE/ASME Transactions on Mechatronics, 4(1), pp. 9–16, 1999. https://doi.org/10.1109/3516.752079

[5] Yang, Y.-P., Luh, Y.-P., Cheung, C.-H. "Design and control of axial-flux brushless DC wheel motors for electric Vehicles-part I: multiobjective optimal design and analysis", IEEE Transactions on Magnetics, 40(4), pp. 1873–1882, 2004. https://doi.org/10.1109/TMAG.2004.828164

[6] Buja, G. S., Kazmierkowski, M. P. "Direct torque control of PWM inverter-fed AC motors - a survey", IEEE Transactions on Industrial Electronics, 51(4), pp. 744–757, 2004. https://doi.org/10.1109/TIE.2004.831717

[7] Hartani, K., Draou, A. "A New Multimachine Robust Based Anti-skid Control System for High Performance Electric Vehicle", Journal of Electrical Engineering and Technology, 9(1), pp. 214–230, 2014. https://doi.org/10.5370/JEET.2014.9.1.214

[8] Sekour, M., Hartani, K., Merah, A. "Electric Vehicle Longitudinal Stability Control Based on a New Multimachine Nonlinear Model Predictive Direct Torque Control", Journal of Advanced Transportation, 2017(1), 4125384, 2017. https://doi.org/10.1155/2017/4125384

[9] Aouadj, N., Hartani, K., Fatiha, M. "New Integrated Vehicle Dynamics Control System Based on the Coordination of Active Front Steering, Direct Yaw Control, and Electric Differential for Improvements in Vehicle Handling and Stability", SAE International Journal of Vehicle Dynamics, Stability, and NVH, 4(2), pp. 119–133, 2020. https://doi.org/10.4271/10-04-02-0009

[10] Yan, R., Li, B., Zhou, F. "Sensorless control of PMSMs based on parameter-optimized MRAS speed observer", In: 2008 IEEE International Conference on Automation and Logistics, Qingdao, China, 2008, pp. 1573–1578. ISBN 978-1-4244-2502-0 https://doi.org/10.1109/ICAL.2008.4636404

[11] Xiang, X., He, Y. "Sensorless operation of PMSM based on hybrid rotor position self-sensing scheme", In: 2007 International Conference on Electrical Machines and Systems (ICEMS), Seoul, South-Korea, 2007., pp. 714–718. ISBN 978-89-86510-07-2 https://doi.org/10.1109/ICEMS12746.2007.4412177

[12] Hartani, K., Maata, F., Merah, A. "Sensorless Master-slave Direct Torque Control of Permanent Magnet Synchronous Motors Based on Speed MRAS Observer in Electric Vehicle", Research Journal of Applied Sciences, Engineering and Technology, 7(23), pp. 5034–5048, 2014. https://doi.org/10.19026/rjaset.7.897

[13] Aouadj, N., Hartani, K., Soltani, A. "DTC Approach of Three Level NPC Inverter PMSM Motor Powertrain Based on MRAS Observer for Electric Vehicles", In: 5th International Conference on Advanced Engineering Technologies, Bayburt, Türkiye, 2024, pp. 291–301. ISBN 978-605-9945-45-5 [online] Available at: https://arsiv2025.bayburt.edu.tr/uploads/.global/icadet/icadet_24_proceedings.pdf [Accessed: 18 October 2024]

[14] Banda, G., Kolli, S. G. "Comparison of ANN- and GA-based DTC eCAR", Journal of Power Electronics, 21(9), pp. 1333–1342, 2021. https://doi.org/10.1007/s43236-021-00273-1

[15] Derbane, A., Tabbache, B., Ahriche, A. "A fuzzy logic approach based direct torque control and five-leg voltage source inverter for electric vehicle powertrains", Revue Roumaine des Sciences Techniques — Série Électrotechnique et Énergétique, 66(1), pp. 15–20, 2021. [online] Available at: https://journal.iem.pub.ro/rrst-ee/article/view/33 [Accessed: 27 December 2021]

[16] El Ouanjli, N., Derouich, A., El Ghzizal, A., Motahhir, S., Chebabhi, A., El Mourabit, Y., Taoussi, M. "Modern improvement techniques of direct torque control for induction motor drives - a review", Protection and Control of Modern Power Systems, 4(2), pp. 1–12, 2019. https://doi.org/10.1186/s41601-019-0125-5

[17] Verma, A., Singh, B., Yadav, D. "Investigation of ANN tuned PI speed controller of a modified DTC induction motor drive", In: 2014 IEEE International Conference on Power Electronics, Drives and Energy Systems (PEDES), Mumbai, India, 2014, pp. 1–6. ISBN 978-1-4799-6372-0
https://doi.org/10.1109/PEDES.2014.7042146

[18] Zhou, Y., Li, S., Zhou, X., Fang, Z. "The control strategy of electronic differential for EV with four in-wheel motors", In: 2010 Chinese Control and Decision Conference, Xuzhou, China, 2010, pp. 4190–4195. ISBN 978-1-4244-5181-4
https://doi.org/10.1109/CCDC.2010.5498381

[19] Draou, A., Hartani, K. "A Novel Direct Torque Control Scheme for PMSM for Improving Quality in Torque and Flux", Renewable Energies & Power Quality Journal, 10(13), 12, 2012.
https://doi.org/10.24084/repqj10.843

[20] Sun, H., Cui, X., Tang, C. "Back-stepping Adaptive SVM Direct Torque Control of SPMSM Drive system", TELEKOMNIKA Indonesian Journal of Electrical Engineering, 12(9), pp. 6587–6593, 2014.
https://doi.org/10.11591/telkomnika.v12i9.5074

[21] Ahmed, T., Kada, H., Ahmed, A. "New DTC strategy of multi-machines single-inverter systems for electric vehicle traction applications", International Journal of Power Electronics and Drive System (IJPEDS), 11(2), pp. 641–650, 2020.
https://doi.org/10.11591/ijpeds.v11.i2.pp641-650

[22] Nurtay, B., Duisenbay, B., Do, T. D. "Direct-Torque Control System Design Using Maximum Torque Per Ampere method for Interior Permanent Magnet Synchronous Motors", In: 2018 ELEKTRO, Mikulov, Czech Republic, 2018, pp. 1–6. ISBN 978-1-5386-4759-2
https://doi.org/10.1109/ELEKTRO.2018.8398286

[23] Li, M., He, J., Demerdash, N. A. O. "A Flux-Weakening Control for Permanent Magnet Synchronous Motors Based on Z-Source Inverters", In: 2014 IEEE Transportation Electrification Conference and Expo (ITEC), Dearborn, MI, USA, 2014, pp. 1–6. ISBN 978-1-4799-2262-8
https://doi.org/10.1109/ITEC.2014.6861776

[24] Direm, C., Hartani, K., Aouadj, N. "New Combined Maximum Torque per Ampere-Flux Weakening Control Strategy for Vehicle Propulsion System", SAE International Journal of Vehicle Dynamics, Stability, and NVH, 5(2), pp. 131–145, 2021.
https://doi.org/10.4271/10-05-02-0009

[25] Norediene, A., Kada, H., Meriem, K., Yassmine, B. "MTPA Flux Weakening Approach for IPMSM Motor Powertrain Used in Vehicle Propulsion System", In:International Conference on Artificial Intelligence in Renewable Energetic Systems (IC-AIRES 2024), Tipasa, Algeria, 2025, pp. 383–394. ISBN 978-3-031-80300-0
https://doi.org/10.1007/978-3-031-80301-7_42

[26] The MathWorks, Inc. "MATLAB 2019, (R2019a)", [computer program] Available at: https://getintopc.com/softwares/development/matlab-2019-free-download-1326503/ [Accessed: 28 March 2019]

[27] Itani, M. K. "Récuperation d'énergie pour système intégré moteur roue, application au véhicule électrique" (Energy recovery for integrated wheel-motor, electric vehicle application), PhD Thesis, Université de Paris-Saclay, 2017. [online] Available at: https://theses.hal.science/tel-01558984v1 [Accessed: 10 July 2017]

[28] Wu, G., Xiao, X. "Speed controller of servo system based on MRAS method", In: 2009 IEEE International Conference on Industrial Technology, Churchill, VIC, Australia, 2009, pp. 1–5. ISBN 978-1-4244-3506-7
https://doi.org/10.1109/ICIT.2009.4939655

[29] Wu, M., Zhao, R., Wang, J. "Sensorless estimation and convergence analysis based on MRAS for PMSM", In: 2010 8th World Congress on Intelligent Control and Automation, Jinan, China, 2010, pp. 1641–1644. ISBN 978-1-4244-6712-9
https://doi.org/10.1109/WCICA.2010.5554717

[30] Kojabadi, H. M., Ghribi, M. "MRAS-based adaptive speed estimator in PMSM drives", In: 9th IEEE International Workshop on Advanced Motion Control, 2006., Istanbul, Türkiye, 2006, pp. 569–572. ISBN 978-1-5090-9421-9
https://doi.org/10.1109/AMC.2006.1631722

[31] Kang, J., Zeng, X., Wu, Y., Hu, D. "Study of Position Sensorless Control of PMSM Based on MRAS", In: 2009 IEEE International Conference on Industrial Technology, Churchill, VIC, Australia, 2009, pp. 1–4. ISBN 978-1-4244-3506-7
https://doi.org/10.1109/ICIT.2009.4939630

[32] An, Q., Sun, L. "On-line Parameter Identification for Vector Controlled PMSM Drives Using Adaptive Algorithm", In: 2008 IEEE Vehicle Power and Propulsion Conference, Harbin, China, 2008, pp. 1–6. ISBN 978-1-4244-1848-0
https://doi.org/10.1109/VPPC.2008.4677634

[33] Liu, J., Wang, X. "Advanced Sliding Mode Control for Mechanical Systems: Design, Analysis and MATLAB Simulation", Springer Berlin, Heidelberg, 2011. ISBN 978-3-642-20906-2
https://doi.org/10.1007/978-3-642-20907-9

[34] Ning, B., Cheng, S., Qin, Y. "Direct torque control of PMSM using sliding mode backstepping control with extended state observer", Journal of Vibration and Control, 24(4), pp. 694–707, 2016.
https://doi.org/10.1177/1077546316650097

[35] Hartani, K., Khalfaoui, M., Merah, A., Aouadj, N. "A Robust Wheel Slip Control Design with Radius Dynamics Observer for EV", SAE International Journal of Vehicle Dynamics, Stability, and NVH, 2(2), pp. 135–146, 2018.
https://doi.org/10.4271/10-02-02-0009